J Mater Sci (2009) 44:3952–3961
DOI 10.1007/s10853-009-3539-z

Numerical studies on columnar-to-equiaxed transition in directional solidification of binary alloys

Arvind Kumar · Pradip Dutta

Received: 9 November 2008 / Accepted: 2 May 2009 / Published online: 26 May 2009

Abstract A numerical study on columnar-to-equiaxed transition (CET) during directional solidification of binary alloys is presented using a macroscopic solidification model. The position of CET is predicted numerically using a critical cooling rate criterion reported in literature. The macroscopic solidification model takes into account movement of solid phase due to buoyancy, and drag effect on the moving solid phase because of fluid motion. The model is applied to simulate the solidification process for binary alloys (Sn–Pb) and to estimate solidification parameters such as position of the liquidus, velocity of the liquidus isotherm, temperature gradient ahead of the liquidus, and cooling rate at the liquidus. Solidification phenomena under two cooling configurations are studied: one without melt convection and the other involving thermosolutal convection. The numerically predicted positions of CET compare well with those of experiments reported in literature. Melt convection results in higher cooling rate, higher liquidus isotherm velocities, and stimulation of occurrence of CET in comparison to the nonconvecting case. The movement of solid phase aids further the process of CET. With a fixed solid phase, the occurrence of CET based on the same critical cooling rate is delayed and it occurs at a greater distance from the chill.

A. Kumar · P. Dutta (✉)
Department of Mechanical Engineering, Indian Institute of Science, Bangalore 560012, India
e-mail: pradip@mecheng.iisc.ernet.in

Present Address:
A. Kumar
Ecole des Mines de Nancy, Parc de Saurupt, 54042 Nancy Cedex, France

Nomenclature

Variables

c_p	Specific heat (J/kg-K)
C	Species concentration (kg/kg)
f	Mass fraction
D	Mass diffusion coefficient of the species (m^2/s)
g	Acceleration due to gravity (m/s^2)
g_l	Volume fraction of liquid
g_s	Volume fraction of solid
G_L	Temperature gradient (K/m)
ΔH	Latent enthalpy content of a control volume (J/kg)
k_p	Partition coefficient
L	Latent heat of fusion (J/kg)
p	Pressure (N/m^2)
r	Cooling rate (K/s)
S	Source term
t	Time (s)
T	Temperature (K)
$\mathbf{u}$	Continuum velocity vector (m/s)
V_L	Tip velocity (m/s)
x, y	Coordinates

Greek symbols

β_T	Thermal expansion coefficient (1/K)
β_C	Solutal expansion coefficient
μ	Dynamic viscosity (kg/s-m)
ρ	Mixture density (kg/m^3)

Subscripts

cr	Critical
eff	Effective
i	Initial
l	Liquid phase

mix Mixture
ref Reference
s Solid phase

Introduction

Metallic alloys exhibit a wide variety of microstructures upon solidification. Among these, dendritic structure, either columnar or equiaxed, is the most common. There is a wide practice of using refiners in the melt for provoking and controlling equiaxed growth in castings [1]. The other mechanism by which equiaxed grains can occur in castings, particularly of nonrefined alloy [2], is the detachment of dendrite arms in the developing mushy zone, which can then be carried into the undercooled melt by bulk flow. In those castings, a columnar-to-equiaxed transition (CET) may occur at a subsequent stage, if the number and size of equiaxed grains ahead of the columnar front become sufficient to stop the columnar growth and subsequently promote the formation of an equiaxed microstructure [3, 4].

The CET during solidification has been studied for many years. Several theories were developed to explain the CET, such as heterogeneous nucleation in the undercooled liquid [3, 5], floatation of grains from the upper surface of the casting, and formation and growth of equiaxed crystals due to thermomechanical fragmentation [6–11]. Among these, fragmentation may give rise to CET if the solid fragments are transported to the columnar front either by liquid flow or by buoyant forces exerting on the detached solid [6–9].

The CET depends on the local solidification parameters such as the temperature gradient in the melt (G_L), the growth velocity of the solidification front (V_L), and the cooling rate (r). Recently, several studies have been reported to model the CET phenomenon, on which a comprehensive review has been presented by Flood and Hunt [10]. These studies have developed expressions or numerical procedures to describe CET criteria which are generally based on tip growth rate and temperature gradient ahead of dendrite tips [12–17]. Hunt and Lu [18] have reported a model for the CET based on metal supercooling, which qualitatively shows the influences of alloy composition, density of nucleating sites, temperature gradient in the melt (G_L), and tip growth rate (V_L). Weinberg and co-workers [15, 16] found that the CET occurs if the temperature gradient (G_L) is sufficiently small. They concluded that lowering G_L increases the likelihood of survival of a nuclei emerging ahead of the columnar front. They also reported that critical values of G_L are in the range 0.1–0.13 K/mm for Pb–Sn alloys and about 0.06 K/mm for Al–3.0wt%Cu, respectively. Suri et al. [14] determined the temperature gradient (G_L) and the liquidus isotherm velocity (V_L) at the CET for solidification experiments in Al–4.5wt%Cu alloys with varying cooling rates and melt superheats. The authors suggested the inequality $G_L < 0.74V_L^{0.64}$ as a criterion for the CET. More recently, Ares and Schvezov [17] have performed directional solidification experiments for Pb–Sn alloys and observed that the CET occurs in a zone rather than in a sharp plane when the temperature gradient in the melt falls below the range 0.8–1.0 °C/cm. Gandin [2], with the help of a solidification model and experiments on directional solidification of Al–Si alloys, proposed a CET criterion based on the position of the maximum velocity of the columnar/dendritic interface. The author predicted a continuous increase in tip growth rate up to a maximum value of about two-thirds the length of the ingot, where the transition is supposed to occur. Wang and Beckermann [19] developed a numerical model to calculate the CET position based on a multiphase approach accounting for the solutal interaction between equiaxed grains. However, in their model, the solutal interaction between the equiaxed grains and the columnar front is neglected, which implies usage of the concept of mechanical blocking to predict the CET. Martorano et al. [4] extended this approach, taking into account the solutal interaction between the equiaxed grains and the columnar front.

Recently, researchers [12, 13] have carried out investigations on vertically upward directional solidification of Al–Cu and Sn–Pb alloys, and proposed a CET criterion based on critical cooling rates. For the combination of initial alloy compositions and cooling conditions used in these experiments, thermosolutal convection was altogether absent. The CET was observed if the cooling rate at the liquidus isotherm (r) becomes less than the critical values of 0.2 K/s for Al–Cu and 0.014 K/s for Sn–Pb alloys [12, 13]. On the same lines, Spinelli et al. [20] carried out an investigation on the CET in Sn–Pb hypoeutectic alloys under conditions favoring thermosolutal convection. The experiments were carried out with cooling conditions causing downward unidirectional solidification. Based on their study, the authors reported a critical cooling rate of about 0.03 K/s for CET.

Li et al. [21] reported that the application of static magnetic field in transforming the microstructure from a mixture of equiaxed and columnar grains to twinned lamellar feathery grains during direct chill casting of Al–9.8wt%Zn alloy. Zuo et al. [22] reported that a new Al–17Si–2.5P master alloy can be successfully used to refine primary Si in hypereutectic A390 alloys. Using a phase-field approach, Tang and Xue [23] studied the growth of interface during directional solidification with different boundary heat fluxes. A model describing the development of dendritic structure and the resulting flow resistance to interdendritic liquid is presented by Oryshchyn and Dogan

[24]. A combination of finite difference method (FDM) for predicting heat flow in a macroscopic scale, and a cellular automata (CA) technique for microscopic modeling of nucleation is presented in [25, 26]. The influence of thermal gradient and growth velocity on CET was investigated and the results were combined on a CET map, showing that a decrease in thermal gradient and an increase in growth rate favor a CET [25]. The model in [26] considered the interaction of concentration fields both within the advancing columnar dendritic network and within the equiaxed grains forming ahead of them.

From the recent studies [12, 13, 20], it is clear that the CET prediction based exclusively on the liquidus isotherm velocity or on the temperature gradient ahead of the liquidus front may not be valid for all ranges of solute compositions for a particular alloy. Instead, a more practical criterion such as a mean value of tip cooling rate can be established as the critical rate at which the microstructural transition occurs for each alloy system. The main purpose of this work is to predict numerically the occurrence of CET in directional solidification of binary alloys, based on the more practical criterion of critical cooling rate, as reported in [12, 13, 20]. Two cooling configurations are studied: one involving solidification of Sn–Pb alloys in a bottom-cooled cavity, where melt convection is absent, and the other involving solidification of Sn–Pb alloys in a top-cooled cavity subjected to thermosolutal convection. The choice of the above cooling configurations and use of same alloy in both cases represent a benchmark test for this numerical study. During solidification, movement of solid crystals (formed from fragmentation of dendritic arms) can play a role in triggering CET. Using the predictions of cooling rates from numerical simulation we intend to highlight the effect of thermosolutal convection and solid movement on the position of CET.

Most mathematical models describing CET take into account the effects of melt convection on the transition. However, there are very few solidification models (such as in [27]) which consider the motion of the detached solid particles. It is revealed in [20] that fluid flow and motion of solid crystals in the mushy zone play an important role in CET. Hence, the present solidification model takes into account solid phase movement due to buoyancy and drag effects. In literature, some of the available models [27, 28] which consider movement of solid phase are based on multiphase approach. Till date, there have been very few attempts on numerical studies of CET with motion of solid phase in a single-phase framework. With this view point, in this study, these effects are incorporated in a single-phase continuum model to study the solidification phenomena under the cooling configurations described earlier. It may be noted that the aim of this work is not to propose any new criterion for CET. Instead, the primary focus of this model is to predict the occurrence of CET using established criteria by considering motion of solid phase along with convective transport in the melt. The model is used to calculate the solidification parameters such as position of the liquidus front, liquidus isotherm velocity, temperature gradient ahead of liquidus, and cooling rate at the liquidus. Predictions for position of liquidus front and cooling rate are then compared with those of experimental data. Thereafter, the cooling rate estimated from the numerical model is used to predict the position of the CET based on a recently reported criterion dealing with critical cooling rate required for the transition. The numerically predicted positions of CET are then compared with the experimentally obtained values available in literature.

Mathematical modeling

The continuum single-phase model for solidification [29–33] is used as a starting point for the current single-domain mixture model which accounts for the movement of solid phase. The continuum mixture relations can be presented as follows:

$$g_l + g_s = 1, \quad f_l + f_s = 1, \quad f_l = \frac{g_l \rho_l}{\rho}, \quad f_s = \frac{g_s \rho_s}{\rho}, \quad \rho = g_l \rho_l + g_s \rho_s \tag{1}$$

$$\vec{u} = f_l \vec{u}_l + f_s \vec{u}_s, \quad k = f_l k_l + f_s k_s, \quad D = f_l D_l + f_s D_s, \quad c_p = f_l c_{p_l} + f_s c_{p_s} \tag{2}$$

Accordingly, the mixture continuity equation is written as:

$$\frac{\partial}{\partial t}(\rho) + \nabla \cdot (\rho \mathbf{u}) = 0 \tag{3}$$

Consideration of the relative phase velocities gives rise to additional terms in momentum and species conservation equations [34–36]. Some of these additional terms require prescription of a solid-phase velocity that is calculated using a simplified model based on Stokes's law, in which force balance is performed on a dendritic particle [34, 37]. In this model, issues such as remelting and growth of solid phase during their motion, resistance offered by moving solid phase, and dependence of viscosity of the solid–liquid mixture on solid fraction are taken into account. To model the flow resistance offered by moving solid phase, a switching function for viscosity is used in the momentum equations. The switching function for viscosity is used after the solid fraction of a control volume reaches a coherency value, beyond which the solid phase becomes immobile. With the activation of the switching function, the effective viscosity model is switched to a Darcy-type source term, which results in a flow through a permeable medium of fixed dendrites [38]. Accordingly, the momentum conservation equations are written as:

X-momentum:

$$\frac{\partial}{\partial t}(\rho u) + \nabla \cdot (\rho \mathbf{u} u) = \nabla \cdot \left(\mu_l \frac{\rho}{\rho_l} \nabla u\right) - \frac{\partial p}{\partial x} - \frac{\mu_l \rho}{K \rho_l} u - \nabla \cdot \left(\mu_l \frac{\rho f_s}{\rho_l} \nabla u\right) + \nabla \cdot (\mu_{\text{eff}} g_s \nabla u) \tag{4}$$

Y-momentum:

$$\frac{\partial}{\partial t}(\rho v) + \nabla \cdot (\rho \mathbf{u} v) = \nabla \cdot \left(\mu_l \frac{\rho}{\rho_l} \nabla v\right) - \frac{\partial p}{\partial y} - \frac{\mu_l \rho}{K \rho_l} v - \nabla \cdot \left(\mu_l \frac{\rho f_s}{\rho_l} \nabla v_s\right) + \nabla \cdot (\mu_{\text{eff}} g_s \nabla v_s) - \nabla \cdot \left[\frac{\rho f_s}{f_l} (\mathbf{u} - \mathbf{u}_s)(v - v_s)\right] - g_s(\rho_s - \rho_l)g + \rho g[\beta_T (T - T_{\text{ref}}) + \beta_C (C_l - C_{\text{ref}})], \tag{5}$$

μ_{eff} appearing in the momentum equations is the effective viscosity and is given as

$$\mu_{\text{eff}} = \mu_l \left[1 - \left(\frac{F_\mu g_s}{0.3}\right)\right]^{-2}, \tag{6}$$

where F_μ is switching function given as $F_\mu = 0.5 - (1/\pi) \tan^{-1}[100\,(g_s - g_{s,cr})]$.

The coherency point beyond which solid cannot move is defined by $g_{s,cr} = 0.27$ [38]. The momentum equations take care of both solid movement and fixed solid (after coherency point). When solid moves, the third term (Darcy term) on RHS of momentum equations is forced to zero. In this case, the resistance offered by solid is taken care by an effective viscosity term (the fifth term on the RHS of momentum conservation equations). After coherency is reached, the third term is made effective, which then acts like a source term for flow through porous medium of fixed dendritic structure. In the third term, K is defined as [38]

$$K = \frac{{g_l}^3}{c(1 - g_l)^2 F_K}, \quad F_K = 1 - F_\mu, \quad c = \frac{180}{{d_2}^2}, \tag{7}$$

where F_K is another switching function used to activate the Darcy term in the momentum equation and d_2 is the secondary dendritic arm spacing in fixed dendritic porous structure. Interactions between the moving solid phase is assumed to increase with increasing solid fraction up to a critical packing fraction, $g_{s,cr}$, where the solid dendrites coalesce to form a rigid structure. The velocity of the moving solid phase is related to the liquid velocity using a simplified model [34, 37] based on Stokes's law for a spherical dendrite particle

$$\mathbf{u}_s - \mathbf{u}_l = \frac{1 - g_s}{18 \mu_{\text{eff}}} (\rho_s - \rho_l) d^2 \mathbf{g}, \tag{8}$$

where d is the characteristic diameter of the moving dendrite particle.

Energy conservation:

$$\frac{\partial}{\partial t}(\rho c_p T) + \nabla \cdot (\rho c_p \mathbf{u} T) = \nabla \cdot (k \nabla T) + \left[\frac{\partial}{\partial t}(\rho f_s L) + \nabla \cdot (\rho f_s \mathbf{u}_s L)\right] - \nabla \cdot [\rho f_s (c_{p_l} - c_{p_s})(\mathbf{u} - \mathbf{u}_s) T], \tag{9}$$

where L is the latent heat of fusion.

Species conservation:

The single-phase transport of the solute equation can be written as:

$$\frac{\partial}{\partial t}(\rho C_{\text{mix}}) + \nabla \cdot [\rho_s g_s \mathbf{u}_s C_s + \rho_l g_l \mathbf{u}_l C_l] = \nabla \cdot (\rho_s g_s D_s \nabla C_s + \rho_l g_l D_l \nabla C_l), \tag{10}$$

where C_{mix} is a representative value obtained by space averaging over a volume defined on the microscopic scale. Representing this microscopic volume by $V = V_s$ (volume of the solid fraction) + V_l (volume of the liquid fraction), the general form of C_{mix} can be written as

$$C_{\text{mix}} = \frac{\int \rho_l C_l \mathrm{d}V_l + \int \rho_s C_s \mathrm{d}V_s}{\rho V} \tag{11}$$

Back diffusion in the solid phase is neglected and Scheil's assumption is made for microscopic diffusion within the solid phase (zero diffusion in solid). The liquid within a representative control volume is assumed to be solutally well mixed. Also, the interface between solid and liquid is assumed to be in local thermodynamic equilibrium. With this assumption and having constant solid and liquid phase density, Eq. 11 becomes

$$\rho C_{\text{mix}} = \rho_l g_l C_l + \rho_s \int_0^{g_s} C_s^* \mathrm{d}\alpha, \tag{12}$$

where C_s^* is the composition of the solid at the interface. According to the thermodynamic equilibrium at the solid–liquid interface, at every value of g_s, C_s^* can be given as $C_s^* = k_p C_l$ where C_l is the local liquid composition at that increment in solid fraction and k_p is the partition coefficient. Defining the integral in the above equation as

$$I = \int_0^{g_s} C_s^* \mathrm{d}\alpha = \overline{C}_s \int_0^{g_s} \mathrm{d}\alpha = \overline{C}_s g_s \tag{13}$$

This integral is computed incrementally by adding the increment corresponding to a change in solid fraction, g_s to the previous value of integrand, I. We used this strategy for both fixed and moving solid phase. The fixed and moving solid phases are distinguished from each other by the

coherency point. Therefore, the distinction between the moving and fixed solid phase will be by the instantaneous value of g_s. The increment can be positive or negative depending on whether the material undergoes solidification or remelting. If solidification has occurred and the increment is positive, I is calculated directly. If there is remelting, however, I must be obtained from the solidification history, with values of g_s and I saved from those of previous time steps. To avoid excessive amount of storage required, g_s and I are not saved at every time step. Instead, I is stored at increments of $g_s = 0.01$, and linear interpolation is used for other values of g_s [39]. Further details on the methodology used to handle remelting are presented in [39]. Now, taking time derivative of the above expression of C_{mix}, one obtains

$$\frac{\partial(\rho C_{mix})}{\partial t} = \frac{\partial(\rho_l g_l C_l)}{\partial t} + \rho_s \overline{C}_s \frac{\partial(g_s)}{\partial t} \tag{14}$$

Substituting the above definition of C_{mix} and its time derivative in the basic equation for transport of C_{mix} (Eq. 10), and casting that equation in the form of C_l, the final conservation equation for species becomes

$$\frac{\partial}{\partial t}(\rho C_l) + \nabla \cdot (\rho \mathbf{u} C_l) = \nabla \cdot (D^+ \nabla C_l) + S_c, \tag{15a}$$

where

$$D^+ = \rho f_l D_l \quad \text{(for Scheil's model)}, \tag{15b}$$

$$S_c = \frac{\partial}{\partial t}[\rho f_s C_l] - \overline{C}_s \frac{\partial}{\partial t}(\rho f_s) - \nabla \cdot (\rho f_s \mathbf{u}_s (C_l - \overline{C}_s)). \tag{15c}$$

Numerical implementation

In the present fixed grid, single-domain continuum formulation, the governing equations of conservation are discretized using a pressure-based finite volume method according to the SIMPLER algorithm [40]. The computational domain is discretized with 80 × 80 elements. The number of grids chosen in the present case ensures sufficient resolution for the problem under consideration and further grid refinement does not change the results appreciably. A time step of 0.1 s is chosen. Convergence in the inner iterations is declared on the basis of relative error of scalar variables to be solved (a tolerance of 10^{-4} is prescribed), as well as on satisfaction of the overall energy balance criteria within a permissible limit of 0.1%.

The model is applied to simulate the solidification process for binary alloys (Sn–Pb) and to estimate solidification parameters such as position of the liquidus, velocity of the liquidus isotherm, temperature gradient ahead of the liquidus, and cooling rate at the liquidus. These solidification parameters are estimated at $g_l = 1.0$ contour. The cooling rate at the liquidus isotherm estimated from the macroscopic scale simulations is used to predict the position of the CET based on a recently reported criterion dealing with critical cooling rate required at the liquidus isotherm for the transition. Since the liquid fraction is calculated from the solution of the coupled governing transport equations in the macroscopic model, local concentration changes and macrosegregation will be inherently reflected in the liquidus isotherm estimated at $g_l = 1.0$ contour. The cooling rate at the liquidus front is evaluated as the rate of change of temperature at that location, which is calculated using the temperatures at the current and previous time steps. The simulations are performed for two cases, one without melt convection and the other involving thermosolutal convection and movement of solid phase. For the no-convection case, the critical cooling rate criterion is evaluated at the liquidus isotherm (i.e., at $g_l = 1.0$ contour). However, for the convective case, this criterion and all other solidification parameters such as, position of the liquidus, velocity of the liquidus isotherm, and cooling rate at the liquidus are evaluated at the coherency point (i.e., at the $g_s = g_{s,cr}$ contour), which separates the immobile columnar phase from the moving equiaxed phase.

Results and discussion

In this study, two cooling configurations have been studied. In the first set of studies, solidification of Sn–20wt%Pb alloy in a bottom-cooled cavity is considered, in which there is no melt convection. The second configuration involves solidification of the same Sn–Pb alloy in a top-cooled cavity which is subjected to thermosolutal convection. The cooling configurations chosen and use of the same alloy for simulation in both cases enable us to highlight the effect of thermosolutal convection and solid movement on the position of CET. The prediction of CET using the present numerical study, which considers movement of solid phase, for the above-mentioned two benchmark cooling configurations and comparison of predicted results with those of experiments, will serve as a test for the model presented.

CET under nonconvecting condition

To study CET in a nonconvecting situation, simulations are performed in a bottom-cooled cavity (same as in [13] with height and width 110 and 50 mm, respectively) for the case of solidification of Sn–20wt%Pb alloy, the schematic for which is shown in Fig. 1. The initial and boundary conditions are taken from [13]. In particular, the initial temperature of the alloy, T_i, is 207 °C and cooling at the bottom chill is prescribed by the mold–metal heat transfer coefficient h_i as a function of time ($h_i = 900\ t^{-0.07}$). The

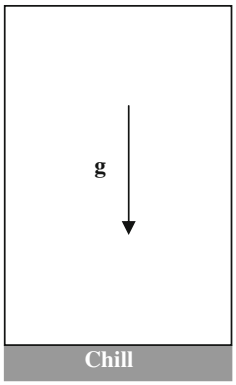

Fig. 1 Schematic of the bottom-cooled solidification system

Table 1 Thermophysical data used in simulations

Parameter	Sn–20wt%Pb
Phase diagram	
Initial mass fraction (wt% Pb)	20
Melting temperature (°C)	232
Eutectic temperature (°C)	183
Eutectic mass fraction (wt% Pb)	39
Liquidus temperature (°C)	202
Thermophysical data	
Specific heat (solid phase) (J kg^{-1} K^{-1})	200
Specific heat (liquid phase) (J kg^{-1} K^{-1})	231
Thermal conductivity (solid phase) (W m^{-1} K^{-1})	59
Thermal conductivity (liquid phase) (W m^{-1} K^{-1})	32
Latent heat of fusion (J kg^{-1})	52,580
Mass density (solid phase) (kg m^{-3})	8250
Mass density (liquid phase) (kg m^{-3})	7860
Thermal expansion coefficient ($°C^{-1}$)	6.0×10^{-5}
Solutal expansion coefficient ($wt\%^{-1}$)	-5.3×10^{-3}
Molecular viscosity (kg m^{-1} s^{-1})	10^{-3}

mold is cooled by water with initial temperature of 25 °C. All other surfaces of the mold are insulated. The data for thermophysical properties, taken from [13], are given in Table 1. With the bottom-cooled cavity for the alloy under consideration, solutal convection is absent as the solute-rich interdendritic liquid is heavier than the overlying melt. At the same time, the melt layer is thermally stable in the bottom-cooled configuration.

Figure 2 shows a comparison of numerically predicted positions of the liquidus front with those of experimental values [13]. Figure 3 shows the variation of cooling rate (estimated as cooling rate at the liquidus isotherm) at the dendrite tip as a function of distance from the chill. A good agreement is observed between the experimental values reported in [13] and those from the present numerical prediction. Subsequently, the predictions from the present numerical model is utilized to estimate relevant solidification parameters associated with CET, such as tip growth rate (V_L), temperature gradient in the liquid ahead of the tip

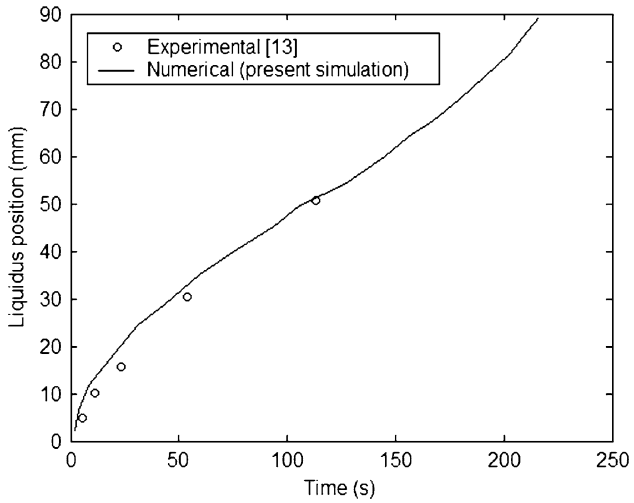

Fig. 2 Comparison of liquidus position from the chill as a function of time

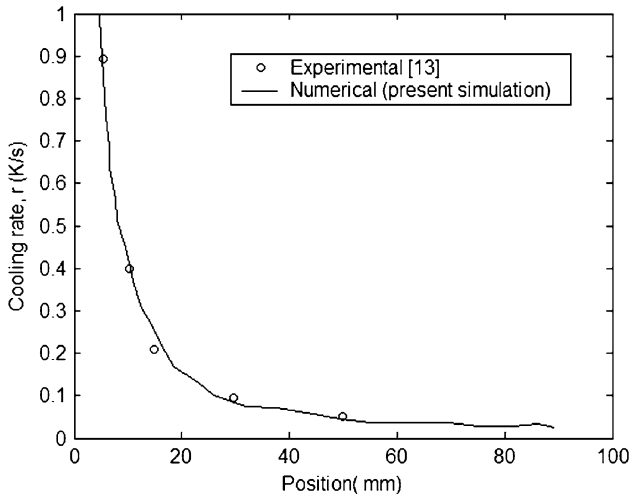

Fig. 3 Comparison of cooling rate at the tip (estimated as cooling rate at the liquidus isotherm) as a function of distance from the chill

(G_L), and the cooling rate (r), as a function of distance from the chill (Figs. 4, 5, 6). It may be noted that due to macroscopic nature of the present model, the tip growth rate and temperature gradient ahead of the tip are approximated as liquidus isotherm velocity and temperature gradient ahead of the liquidus isotherm, respectively. For unidirectional heat flow conditions in the present simulation, the tip growth rate first decreases from the chill face to the interior of the ingot, and increases again towards the other end of the ingot. The first decrease in the growth rate is due to reduction in cooling away from the chill (see Fig. 3). Toward the end of solidification (near the other end of the ingot), however, the end effects play a major role on tip growth rate (Fig. 4). Such end effects are also observed experimentally (for example, see [12]). Toward the end of solidification, there is an increase in the growth rate

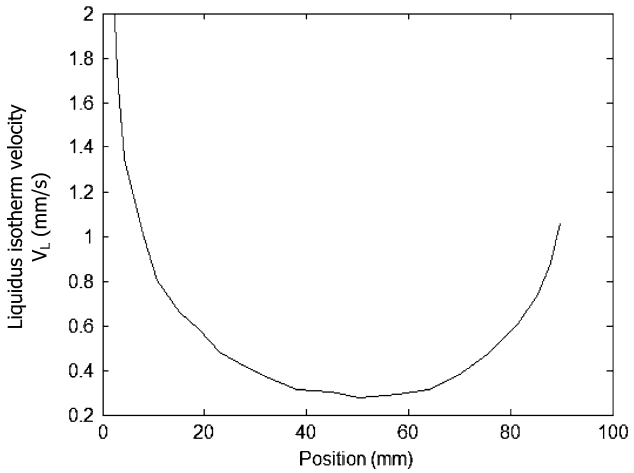

Fig. 4 Tip velocity (estimated as liquidus isotherm velocity) as a function of distance from the chill

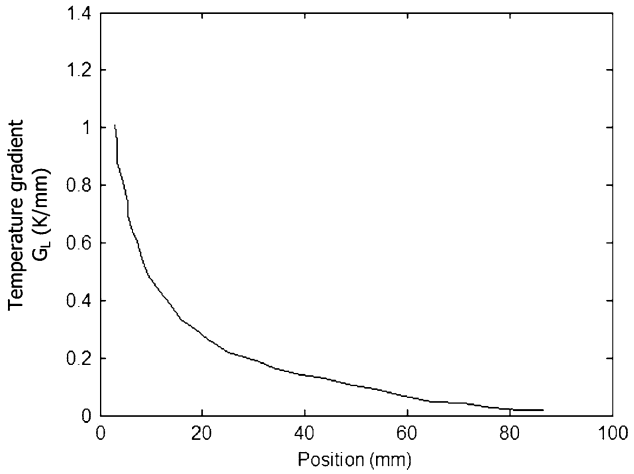

Fig. 5 Temperature gradient at the tip (estimated as gradient at the liquidus isotherm) as a function of distance from the chill

because of progressive reduction in latent heat evolution. Figure 5 shows a gradual decrease of temperature gradient with distance from the chill. A similar decreasing trend (with distance from the chill) is also observed for the case of cooling rate (Fig. 6). The experimentally reported and numerically predicted positions of CET, based on the criterion of critical cooling rate ($r < 0.014$ K/s for Sn–Pb alloys [13]), are also marked on this figure. The numerical prediction for the position of CET (68 mm) compares reasonably well with that of the experiments (65 mm).

CET under convecting condition

CET in convecting situation is studied by carrying out simulation in a top-cooled cavity (same as in [13] with height and width 150 and 56 mm, respectively), the

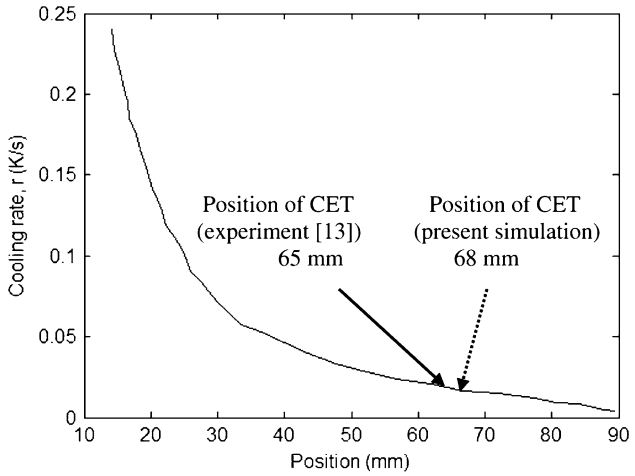

Fig. 6 Variation of cooling rate at the tip (estimated as cooling rate at the liquidus isotherm) with distance from the chill. The experimentally reported and numerically obtained positions of CET based on critical cooling rate are marked

Fig. 7 Schematic of the top-cooled solidification system

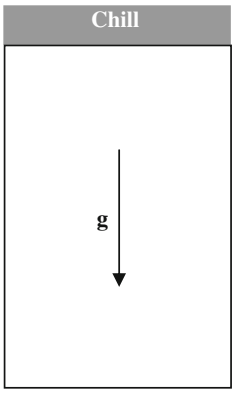

schematic for which is shown in Fig. 7. The simulation is carried out for solidification of the same alloy (Sn–20wt%Pb alloy), as in the previous case. The initial and boundary conditions are taken from [20]. In this case, however, the initial temperature of the alloy, T_i, is 211 °C and cooling is prescribed by the mold–metal heat transfer coefficient h_i as a function of time ($h_i = 2100\, t^{-0.001}$). The mold is cooled by water with initial temperature of 25 °C and all other sides of the mold are insulated.

Snapshots of simulated results showing velocity field and solid fraction distribution are shown in Fig. 8. The rejection of heavier solute (Pb in this case) into the melt during solidification and the temperature gradients set by the top-cooled configuration will induce thermosolutal convection. The contour of coherency point ($g_{s,cr} = 0.27$) is superimposed on the solid fraction distribution. The effect of convection is observed in the shape of the solidifying fixed mushy zone which is wavy in this case. As observed in Fig. 8, the moving solid phase is drifted by

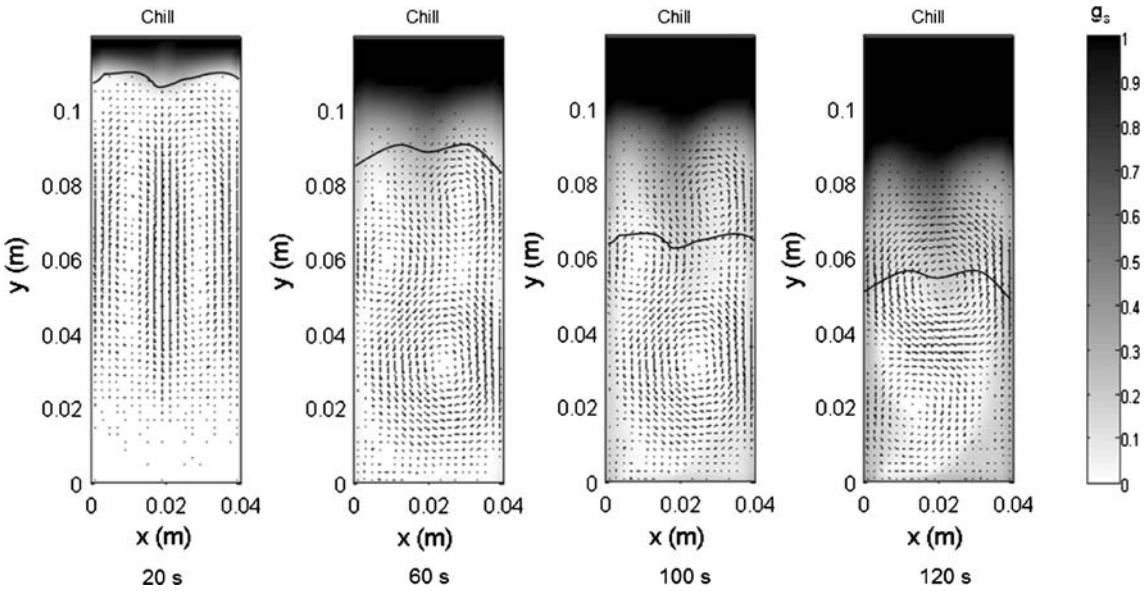

Fig. 8 Simulation results showing velocity vectors and solid fraction distribution. The lines superimposed show the contour of coherency point ($g_{s,cr} = 0.27$)

convective currents and a portion of the solid phase may also sink toward the bottom of the cavity. In this manner, some of the solid phase may again be brought back toward the columnar phase front by convection, thus restricting the columnar front growth. The solid phase is spread over the whole cavity when solidification in the cavity has progressed up to 70 mm from the chill, and CET may occur.

For the convective case, all the solidification parameters, such as position of the liquidus, velocity of the liquidus isotherm, and the critical cooling rate, are evaluated at the coherency point which separates the columnar phase from the equiaxed phase. It may be noted that these parameters are estimated at the mid-width of the cavity. Figure 9 shows the calculated tip velocity (estimated as isotherm velocity at $g_s = g_{s,cr}$) as a function of downward distance from the chill. There is good agreement between numerical predictions and experimentally obtained values. The variation of cooling rate at the columnar tip (estimated as cooling rate at the isotherm at $g_s = g_{s,cr}$) with downward distance from the chill is shown in Fig. 10. On comparing Figs. 3 and 10, it can be noticed that in presence of convection, relatively higher cooling rates are achieved. The predicted cooling rate is in good agreement with the experimental values. The experimentally reported and numerically predicted positions of CET, based on the criterion of critical cooling rate ($r < 0.03$ K/s for Sn–Pb alloys [20]), are marked on Fig. 10. The numerical prediction for CET (79 mm) compares reasonably well with the corresponding experimentally obtained value (76 mm). With convection, the CET is stimulated as it occurs at a higher critical cooling rate ($r = 0.03$ K/s [20]) than that

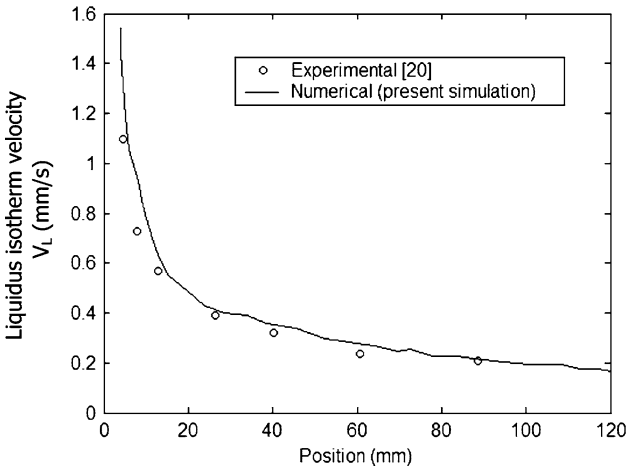

Fig. 9 Tip velocity (estimated as isotherm velocity at $g_s = g_{s,cr}$) as a function of distance from the chill

observed during nonconvecting situation for solidification of Sn–Pb alloys ($r = 0.014$ K/s [13]). Due to large variation of the cooling rate (0.02–2 K/s) in the cavity, the cooling rate variation with position seems almost parallel to the axis. However, with better resolution after changing the scale of the axis, the variation no longer appears to be parallel to the axis. The position of occurrence of critical cooling rate is carefully predicted after sufficiently magnifying Fig. 10 around the critical cooling rate.

To highlight the effect of movement of solid phase on CET, simulation is also performed considering a case in which the solid phase is fixed. With a fixed solid phase, the occurrence of CET based on the same critical cooling rate

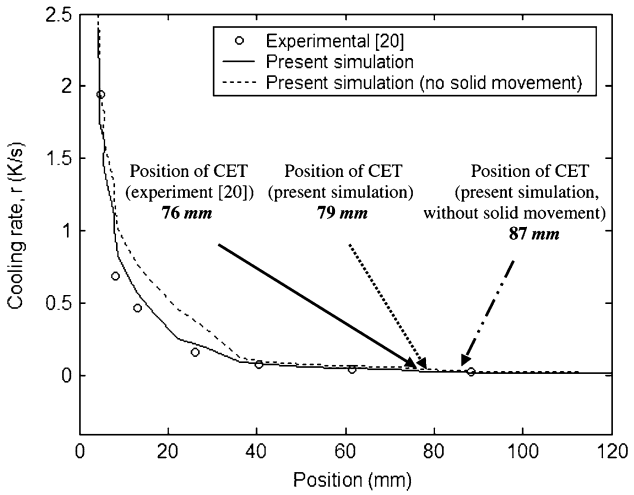

Fig. 10 Variation of cooling rate at the tip estimated as cooling rate at the isotherm at $g_s = g_{s,cr}$) with distance from the chill. The experimentally reported and numerically obtained positions of CET based on critical cooling rate are marked

is delayed and it occurs at a greater distance from the chill (i.e., at 87 mm) as shown in Fig. 10. Hence, in the present case, the movement of solid phase is found to aid the process of transition. The stimulation of occurrence of CET in moving solid phase case is due to filling of the whole cavity by the moving solid phase, thus restricting the growth of the columnar phase.

It may be noted that the immobile columnar phase is demarcated from the mobile equiaxed phase by the coherency point ($g_{s,cr} = 0.27$, in the present case). In literature [34, 38], the same value of coherency point is used. The coherency point may depend on the specific alloy and the microstructure. However, for the purpose of illustration, a value of 0.27 is chosen for the present simulations. To assess the effects of coherency point chosen on the CET, a parametric study for the occurrence of CET is performed by varying the coherency point, and the result is summarized in Table 2. The computations are performed with two other values of coherency points, one greater ($g_{s,cr} = 0.4$) and the other less ($g_{s,cr} = 0.1$) than the nominal value of 0.27. It is found that the occurrence of CET is stimulated with higher coherency point value. With more solid phase movement possible with higher coherency point, more solid phase is brought back toward the columnar phase by convection, thus restricting its growth and stimulating CET.

It is reported in [13] and [20] that the position of CET based on the critical cooling rate is valid for all experimental conditions, irrespective of the composition of Sn–Pb alloys, mold–metal heat transfer coefficient, and superheat. A good comparison with those of experiments illustrates the capability of the present model which also considers movement of solid phase. This model can be used to predict CET for other alloys systems, too, based on appropriate critical cooling rate criteria.

It may be noted that in this work, fragmentation and detachment are not considered. Fragmentation of the dendrite arms is a complex structural phenomenon and its integration into a macroscopic solidification model in a physically consistent manner is beyond the scope of the present model.

Conclusion

A numerical study for CET based on established critical cooling rate criterion is presented. The macroscopic model presented in this study considers motion of solid phase due to gravity and viscous drag in a single-phase framework. The model is used to calculate the solidification parameters, such as position of the liquidus front, velocity of the liquidus isotherm, temperature gradient ahead of the liquidus, and cooling rate at the liquidus isotherm, for two cooling configurations. Numerical predictions are made for the position of CET, based on the critical cooling rate criterion. The predictions are compared with the results available in literature, and a good agreement is observed. In the convecting situation, the predictions show the effect of melt convection on the solidification behavior in terms of a wavy-shaped fixed mushy zone, higher cooling rate, and higher liquidus isotherm velocities, in comparison to the nonconvecting case. The predictions are in line with experimental results reported in literature, in that the occurrence of CET is stimulated by melt convection and transport of solid crystals. The present model can also be used for solidification in more generalized cases (say, in a side-cooled cavity, provided the data about critical cooling rate criterion is available), and for other alloy systems. The

Table 2 Effect of coherency point chosen on CET

	Experiment [20]	Simulations			
		Fixed solid phase	Moving solid phase		
			$g_{s,cr} = 0.1$	$g_{s,cr} = 0.27$	$g_{s,cr} = 0.4$
CET position—distance from the chill (mm)	76	87	83	79	78

model can be further used to investigate the influences of solute concentration, melt superheat, cooling configurations, and metal–mold heat transfer coefficients on the CET position.

Acknowledgement The authors gratefully acknowledge the financial support of General Motors Corporation, USA.

References

1. Quested TE, Greer AL (2005) Acta Mater 53:4643
2. Gandin CA (2000) Acta Mater 48:2483
3. Hunt JD (1984) Mater Sci Eng 65:75
4. Martorano MA, Beckermann C, Gandin CA (2003) Metall Mater Trans A 34:1657
5. Mathiesen R, Arnberg L, Ramsoskar K, Weitkamp T, Rau Ch, Snigirev A (2002) Metall Mater Trans B 33:613
6. Kumar A, Dutta P, Rayleigh A (2008) J Phys D 41:155501, 9 pp
7. Mathiesen RH, Arnberg L, Bleuet P, Somogyi A (2006) Metall Mater Trans A 37:2515
8. Griffiths WD, Xiao L, McCartney DG (1996) Mater Sci Eng A 205:31
9. Kumar A, Dutta P (2006) J Phys D 39:3058
10. Flood SC, Hunt JD (1988) Metals handbook, vol 15. ASM International, Materials Park, p 130
11. Herlach DM, Eckler K, Karma A, Schwarz M (2001) Mater Sci Eng A 304–306:20
12. Siqueira CA, Cheung N, Garcia A (2002) Metall Mater Trans A 33:2107
13. Siquiera CA, Cheung N, Garcia A (2003) J Alloys Compd 351:126
14. Suri VK, El-Kaddah N, Berry JT (1991) AFS Trans 99:187
15. Mahapatra RB, Weinberg F (1987) Metall Trans B 18:425
16. Ziv I, Weinberg F (1989) Metall Trans B 20:731
17. Ares AE, Schvezov CE (2000) Metall Mater Trans A 31:1611
18. Hunt JD, Lu SZ (1996) Metall Mater Trans A 27:611
19. Wang CY, Beckermann C (1994) Metall Mater Trans A 25:1081
20. Spinelli JE, Ferreira IL, Garcia A (2004) J Alloys Compd 384:217
21. Li L, Zhang Y, Esling C, Zhao Z, Zuo Y, Zhang H, Cui J (2009) J Mater Sci 44(4):1063. doi:10.1007/s10853-008-3158-0
22. Zuo M, Liu X, Sun Q (2009) J Mater Sci 44(8):1952. doi:10.1007/s10853-009-3287-0
23. Tang J, Xue X (2009) J Mater Sci 44(3):745. doi:10.1007/s10853-008-3157-1
24. Oryshchyn DB, Dogan ON (2008) J Mater Sci 43(4):1471. doi:10.1007/s10853-007-2325-z
25. Dong HB, Yang XL, Lee PD, Wang W (2004) J Mater Sci 39(24):7207. doi:10.1023/B:JMSC.0000048733.96958.c3
26. Dong HB, Lee PD (2005) Acta Mater 53(3):659
27. Ludwig A, Wu M (2005) Mater Sci Eng A 413–414:109
28. Appolaire B, Combeau H, Lesoult G (2008) Mater Sci Eng A 487(1–2):33
29. Bennon WD, Incropera FP (1987) Int J Heat Mass Transf 30(16):2161
30. Voller VR, Brent AD, Prakash C (1989) Int J Heat Mass Transf 32(9):1719
31. Prescott PJ, Incropera FP (1996) In: Poulikakos D (ed) Advances in heat transfer, vol 28. Academic Press, New York, pp 231–338
32. Voller VR (2006) In: Minkowycz WJ, Sparrow EM, Murthy JY (eds) Handbook of numerical heat transfer, 2nd edn. Wiley, New York, chap 19
33. Kumar A, Dutta P (2005) Int J Heat Mass Transf 48:3674
34. Vreeman CJ, Krane MJM, Incropera FP (2000) Int J Heat Mass Transf 43:677
35. Chowdhury J, Ganguly S, Chakraborty S (2005) J Phys D 38:2869
36. Chowdhury J, Ganguly S, Chakraborty S (2007) Int J Heat Mass Transf 50:2692
37. Manninen M, Taivassalo V, Kallio S (1996) On the mixture model for multiphase flow. VTT Publications 288, Technical Research Centre of Finland, Espoo
38. Yang BJ, Leon-Torres J, Stefanescu DM (1999) Int J Cast Met Res 11:527
39. Kumar A, Dutta P, Walker MJ, Sundarraj S (2007) Numer Heat Transf A 51:59
40. Patankar SV (1980) Numerical heat transfer and fluid flow. Hemisphere, Washington, DC